Isotope effects on transport characteristics of edge and core plasmas heated by neutral beam injection (NBI) in an inward shifted configuration at the Large Helical Device

PAPER • OPEN ACCESS

Isotope effects on transport characteristics of edge and core plasmas heated by neutral beam injection (NBI) in an inward shifted configuration at the Large Helical Device

To cite this article: H. Zhou *et al* 2024 *Nucl. Fusion* **64** 036023

OPEN ACCESS
IOP Publishing | International Atomic Energy Agency
Nuclear Fusion
Nucl. Fusion **64** (2024) 036023 (16pp)
https://doi.org/10.1088/1741-4326/ad22f6

Isotope effects on transport characteristics of edge and core plasmas heated by neutral beam injection (NBI) in an inward shifted configuration at the Large Helical Device

H. Zhou[1], Y. Xu[1,*], M. Kobayashi[2,3,*], A. Shimizu[2,3], R. Seki[2], K. Tanaka[2], T. Tokuzawa[2,3], M. Yoshinuma[2,3], Y. Takemura[2,3], H. Takahashi[2,3], K. Ogawa[2,3], J. Cheng[1], W. Li[1], D.N. Wu[1], Y.J. Zhu[1], Y. Luo[1], Y.C. Li[1], J. Huang[1], X.Q. Wang[1], H.F. Liu[1], H. Liu[1] and X. Zhang[1]

[1] Institute of Fusion Science, School of Physical Science and Technology, Southwest Jiaotong University, Chengdu 610031, China
[2] National Institute for Fusion Science, National Institutes of Natural Sciences, Toki, Gifu 509-5292, Japan
[3] National Institute for Fusion Science, The Graduate University for Advanced Studies, SOKENDAI, Toki, Gifu 509-5292, Japan

E-mail: xuyuhong@swjtu.edu.cn and kobayashi.masahiro@nifs.ac.jp

Received 26 September 2023, revised 9 January 2024
Accepted for publication 26 January 2024
Published 13 February 2024

Abstract

Isotope effects have been investigated in Neutral Beam Injection (NBI) heated plasmas on the Large Helical Device with similar operational parameters between Hydrogen (H) and Deuterium (D) plasmas. Experimental results show that the global energy confinement has no significant dependence on the isotope mass under similar discharge conditions with nearly the same heating power, line-averaged density ($\bar{n}_e$) and magnetic field. For both electron and ion energy transport, the transport coefficients, which are obtained based on local power balance analysis, have analogous profiles between H and D dominant plasmas. For neoclassical χ_e and χ_i values, they are almost equal between H and D dominant plasmas in low $\bar{n}_e$ discharges, whereas in high $\bar{n}_e$ cases they are lower in H plasmas than those in D ones. At low $\bar{n}_e$, the electron and ion thermal transport in both H and D plasmas are dominated by neoclassical transport at a certain zone ($\rho \approx 0.6 - 0.85$), while the anomalous transport process has primary effects in the remaining area, and the density fluctuations exhibit ion temperature gradient mode nature. With increase of $\bar{n}_e$, the anomalous transport becomes prevailing and the density fluctuations propagate along electron diamagnetic drift direction. Bispectral analysis reveals that the H plasma has

* Authors to whom any correspondence should be addressed.

stronger nonlinear coupling in edge density fluctuations in both low and high density discharges, which is probably due to that the D plasma has stronger damping rate for the nonlinear interaction of turbulence. For a comparative study, the present results have been compared with those observed in the ECRH discharges (Tanaka *et al* 2019 *Nucl. Fusion* **59** 126040). The reasons for the similarities and dissimilarities between these two different heating manners are not clear yet. To unravel the underlying physics, essential inputs from theories and simulations are required.

Keywords: isotope effects, NBI-heated plasmas, confinement, turbulence transport

(Some figures may appear in colour only in the online journal)

1. Introduction

One of key issues in fusion research is to understand the isotope mass effect on plasma confinement for predicting the performance of the Deuterium (D) and Tritium (T) operation in the fusion reactor. In recent years, the isotope effects have attracted much attention and a large number of experimental studies have been implemented in various fusion devices [1]. In tokamaks [2–6], there were numerous experimental evidences that the confinement properties in D plasmas is better than in Hydrogen (H) ones at comparable plasma discharge parameters, which is not in accordance with the gyro-Bohm scaling for which the plasma diffusivity is proportional to the square root of the ion mass (M_i) [7, 8]. However, some different results also showed up in tokamak devices, e.g. in the JET-ILW experiment and the L-mode discharge at DIII-D the thermal energy confinement time (τ_{th}) is weakly dependent upon the isotope mass [5, 9], and in the ELM-free H mode on JET the τ_{th} even decreases with the isotope mass ($\tau_{th} \sim M_i^{-0.25}$) [10]. In the RFX-mod reversed field pinch device, it has been seen that the energy and particle confinement times scaled with M_i as $\tau_{th} \sim M_i^{0.3}$ and $\tau_p \sim M_i^{0.45}$, respectively [11]. In stellarators, the isotope mass effects on confinement properties appear also diverse in different machines. In the early stage, comparative studies in the L-mode discharges among ATF, CHS, Heliotron E heliotrons and W7-A and W7-AS stellarators indicated that the energy confinement depends very weakly on the ion mass [4]. In the Large Helical Device (LHD), a statistical regression analysis for the H and D plasmas heated by the Neutral Beam Injection (NBI) under different discharge parameters has yielded a τ_{th} scaling, which shows no significant dependence on M_i [12]. But in electron cyclotron resonant heating (ECRH) H and D plasmas with the same line-averaged density and heating/absorbed power at LHD, it has been found that the τ_{th} in D plasmas is better than in H ones, while τ_p is worse in D plasmas [13]. In the CHS device, it is observed that the isotope effect on τ_p is associated with plasma density. In case of low density discharges the τ_p is better in D plasmas, whereas in high density regime the τ_p is nearly equal in H and D dominant plasmas [14]. In Heliotron J, it has been found that both of the particle diffusivity and inward convection are higher in H plasmas than in D ones [15].

On the other hand, the importance of multiscale physics, such as turbulence and zonal flows, in isotope effects have been identified experimentally in tokamaks and stellarators [2, 6, 16–24]. Experimental results revealed that transport properties and turbulence modes, e.g. Ion Temperature Gradient mode (ITG) and Trapped Electron Mode (TEM), may both vary depending on collisionality and the T_e/T_i ratio [25, 26], in agreement with the theoretical and simulation results [27].

All above results indicate that the isotope effects on plasma transport and confinement are rather diverse and complicated, depending on magnetic configurations and discharge conditions in various devices. Therefore, it is imperative to thoroughly understand the influence of the isotope mass on the plasma confinement, transport and fluctuation characteristics from the existing experimental database for improving the performance of D–T operation in fusion reactors. In LHD, a careful comparison of the isotope effect has been conducted in terms of dimensionally similar parameters, ρ_*, ν_*, β, as mentioned above [12]. Isotope effects between the ECR-heated H and D plasmas has been carried out under the same discharge conditions [13]. In the present work, we revisit the isotope effects of NBI heated plasmas in terms of global confinement with heat transport analysis based on the local power balance obtained from the experimental profiles for similar operational parameters between H and D plasmas, such as n_e, $T_{e,i}$, P_{abs}, B. The operational parameters are also crucial for prediction from the engineering point of view (e.g. magnetic field and heating power) as well as achievable fusion power which is a function of the operational parameters, density and temperature, etc. By assessing neoclassical transport, we deduce the contribution from anomalous transport in relation to the fluctuation measurements. We also investigate edge fluctuation characteristics, which are important for the plasma-wall interaction as well as core-edge coupling of transport, for which we observed clear difference between H and D plasmas. This paper particularly addresses the inward shifted configuration of LHD, where neoclassical transport is optimized. This is also due to the data availability at present. The analysis on other magnetic configurations is underway and published elsewhere.

The rest of the paper is organized as follows: section 2 gives description of the experimental setup and main diagnostics. Section 3 presents the experiment results, including the energy

transport and turbulence characteristics. Finally, a summary is given in section 4.

2. Experimental setup

LHD is a large superconducting heliotron-type device with a major radius $R_0 = 3.9$ m and an averaged minor radius $a \sim 0.6$ m. In the present study, the NBI-heated experiments were conducted in the 23rd experimental campaign and the plasma parameters were as follows: the toroidal magnetic field $B_T = 2.75$ T, the magnetic axis position was fixed at $R_{ax} = 3.6$ m and the magnetic field direction of Counter-Clockwise, which is the typical configuration in LHD. In order to explore the impact of different heating powers and plasma densities on the isotope effects in the H-majority (H content $\approx 67\%$) and D-majority (D content $\approx 72\%$) plasmas on plasma transport properties, we have made a scan of the NBI heating power in a range of 7–12 MW, and the line-averaged densities ($\bar{n}_e$) in a range of $(1.5-4.5)\times10^{19}$ m^{-3} during the experiments. The rest of the percentage of the species is deuterium (or hydrogen) for hydrogen (or deuterium) dominant discharges, with small amount of helium that is introduced for the purpose of diagnostics. For the line-averaged density, an excellent feedback control of the fuel gas ensured that the H- and D-dominant plasmas have approximately the same value of $\bar{n}_e$ in compared discharges. For the NBI heating, three tangentially injected neutral beam heating systems [28] have been utilized in the experiment. Although the NBI port-through powers in H and D plasmas is slightly different, the deposited power, which is evaluated by the NB shine-through measurement as shown in [29], is almost the same in compared discharges. In addition, a perpendicular NBI was employed for the Charge Exchange Spectroscopy (CXRS) to measure radial profiles of the ion temperature (T_i), radial electric field (E_r) and the poloidal rotation velocity ($V_{E\times B}$) [30]. The profiles of electron density (n_e) and temperature (T_e) were measured by the YAG laser Thomson scattering (TS) [31], and the density fluctuation amplitude and phase velocity (V_{ph}) were measured by a Two-Dimensional Phase Contrast Imaging system (2D-PCI) [32]. The frequency and wavenumber ranges detected by the 2D-PCI are 20–500 kHz and 0.1–0.8 mm^{-1}, respectively. In this experiment, the accessible region of the PCI is about $\rho = 0.4$–1.2. In addition, the edge density fluctuation ($\tilde{n}_e$) is measured by Ka-band Microwave frequency comb Doppler reflectometer system [33, 34], the eight fixed probing frequencies (27.7, 29.1, 30.5, 32.0, 33.3, 34.8, 37.0, 38.3 GHz) of reflectometer correspond to varying cut-off densities from small to large.

3. Experimental results and discussions

3.1. Comparison of energy transport between isotopic H- and D-dominant plasmas

In this study, experiments for the comparison of energy transport between the H- and D-dominant plasmas were executed under similar values of the NBI deposited power and the line-averaged density. Figures 1(*a*)–(*d*) plot typical discharge waveforms in H (#176305) and D (#171617) majority plasmas of high NBI power discharges. Figures 1(*a*) and (*b*) show that the two discharges have nearly the same line-averaged density ($\bar{n}_e = 4.5\times10^{19}$ m^{-3}) and NBI deposited power ($P_{NBI} = 10$ MW). During the stationary discharge phase ($t = 4$–4.5 s), figure 1(*c*) shows that the plasma stored energy (W_p) measured by the diamagnetic loop in H majority plasmas is almost equal to that in the D ones. This implies that the H- and D-dominant plasmas have comparable energy confinement under similar discharge conditions. The diamagnetic energy confinement time ($\tau_{E,dia}$) for the H- and D-dominant plasmas can be estimated by $\tau_{E,dia} = W_p/(P_{NBI} - dW_p/dt)$. The results are depicted in figure 1(*d*). Note that in figure 1(*c*) the abrupt jumps in the W_p signals were caused by the perpendicular injection of positive NBI for CXRS diagnostic at 4, 4.5 and 5 s.

Figures 1(*e*)–(*g*) plot the profiles of plasma density (n_e), electron and ion temperatures (T_e, T_i) as well as the electron pressure ($P_e = n_eT_e$) for H- and D-dominant plasmas at $t \approx 4$ s, at which the T_i profile measured by the CXRS is available. In these figures, points are raw data and the lines represent fitted curves. It is seen that for the present discharge conditions the T_i in the H and D plasmas is approximately equal (see figure 1(*f*)). In the outer plasma region ($\rho > 0.6$) the D plasma generally has higher n_e and T_e than the H ones. However, in the inner plasma region ($\rho < 0.6$) the T_e is higher and the n_e is lower in D plasmas, resulting in no significant difference in P_e for H and D majority plasmas. These profiles confirm that the H plasma has comparable energy confinement to D plasma.

Figure 2(*a*) further summarizes the $\tau_{E,dia}$ values estimated in H- and D-discharges with various NBI heating powers and line-averaged densities as a function of the normalized collisionality (ν^*_{ei}) measured at the normalized radius $\rho = 2/3$. The normalized collisionality is defined as $\nu^*_{ei} = \nu_{ei}/(\varepsilon_{\rm eff}^{\frac{3}{2}} v_{th}\iota/R_0)$ [35, 36]. Here, ν_{ei}, $\varepsilon_{\rm eff}$, v_{th}, ι and R_0 are the electron–ion collision frequency, effective helical ripple, electron thermal speed, rotational transform, and major radius of the torus. All parameters are evaluated at $\rho = 2/3$ as a representative location. The results show that (i) the $\tau_{E,dia}$ values generally increase with increasing ν^*_{ei}; (ii) in either high or low NBI heating scenario the diamagnetic energy confinement time is nearly the same between H and D plasmas at each comparable ν^*_{ei}. Because the diamagnetic stored energy may include effects of fast ions, we have also calculated the kinetic energy confinement time $\tau_{E,kin}$ of those shots from n_e, T_e and T_i profiles [37]. For comparison, the $\tau_{E,kin}$ values at $\rho = 2/3$ are illustrated in figure 2(*c*) as a function of ν^*_{ei}, which exhibits very similar features to those in figure 2(*a*). Figures 2(*b*) and (*d*) show the collisionality dependence of the confinement enhancement factors, which is equal to energy confinement time divided by ISS04 scaling. ISS04 scaling is defined as $\tau_E^{ISS04} = 0.134a^{2.28}R^{0.64}P^{-0.61}\bar{n}_e^{0.54}B^{0.84}\iota_{2/3}^{0.41}$ [38]. The results explicitly indicate that the global energy confinement has no significant dependence on the isotope mass in the present NBI heating discharges under comparable discharge parameters at LHD. The above result is consistent with the study by Yamada

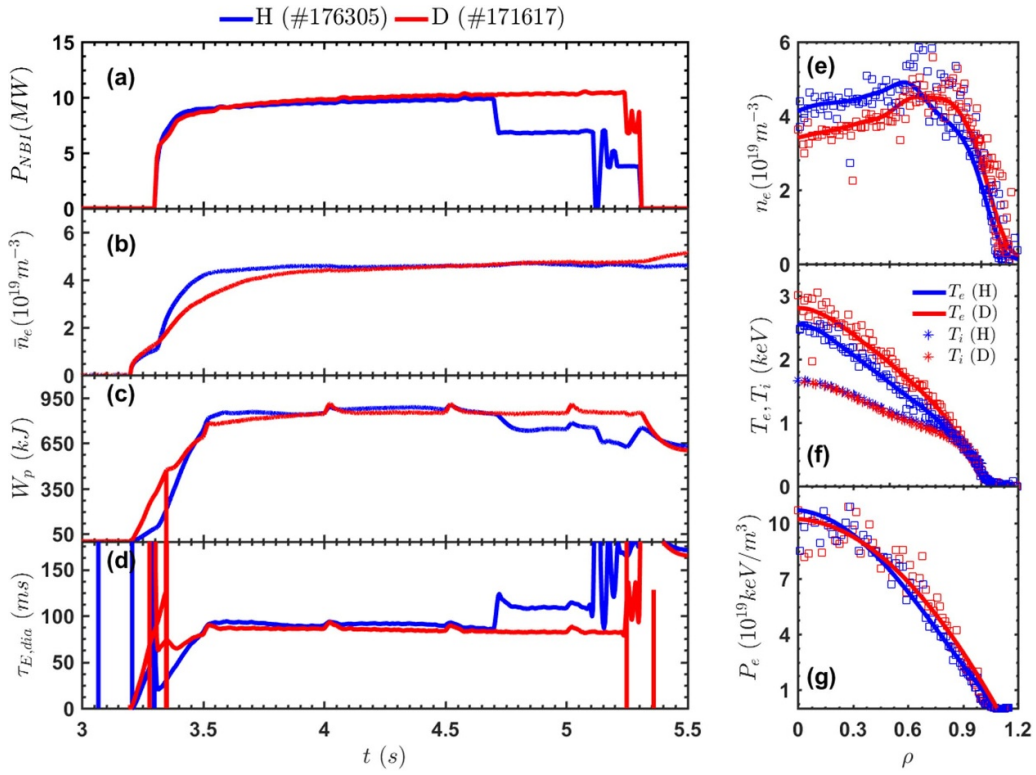

Figure 1. Typical discharge waveforms in H (#176305) and D (#171617) majority plasmas of high power NBI discharges. (*a*) Absorpted/deposited heating power (P_{NBI}); (*b*) line-averaged density ($\bar{n}_e$); (*c*) plasma stored energy (W_p); (*d*) diamagnetic energy confinement time ($\tau_{E,dia}$); (*e*)–(*g*) show radial profiles of electron density (n_e), electron and ion temperatures (T_e, T_i) and the electron pressure ($P_e = n_e T_e$) for H (blue color) and D (red color) dominant plasmas at t ≈ 4 s.

et al on isotopic effects in NBI heating based dimensionally similar plasmas in terms of ρ_*, ν_*, β [12], On the other hand, the present results are very different from those observed in the ECRH heated H- and D-dominant plasmas at LHD, where the energy confinement time is lower in H plasmas than D ones with similar heating power and the line-averaged density [13]. In addition, figure 2 shows that the energy confinement time in both H and D discharges are systematically lower in higher $P_{\rm NBI}$ cases, consistent with the ISS04 scaling of $\tau_E \propto P^{-0.61}$.

In order to understand the impact of the NBI deposited power and plasma density on the energy transport characteristics of the isotopic H and D plasmas, we have compared the radial profiles of n_e, T_e and T_i together with the experimental thermal transport coefficients χ_e and χ_i calculated by the TASK3D code based on the local power balance analysis [39]. The transport coefficient χ is defined as follows:

$$\chi_j = -\frac{\int P_j V' \mathrm{d}\rho}{\langle|\nabla\rho^2|\rangle V' n_j \frac{\partial T_j}{\partial \rho}} \tag{1}$$

where j denotes species, and ρ, n_j, T_j and P_j are minor radius, density, temperature and the heat source, which is defined as,

$$P_e = -\frac{n_e T_e}{\tau_{ei}} + \frac{n_i T_i}{\tau_{ie}} + P_{nbe} \tag{2}$$

$$P_i = \frac{n_e T_e}{\tau_{ei}} - \frac{n_i T_i}{\tau_{ie}} + P_{nbi}. \tag{3}$$

Here P_{nbe} and P_{nbi} denotes the heating power of NBI for electrons and ions, respectively. The first and the second terms are energy equilibration between electrons and ions, and $V' = \partial V/\partial\rho$. We have used the transport coefficient χ for the transport analysis since the heat flux cannot be directly measured in experiments. This is also the same for all previous transport analysis in LHD listed in the references. Therefore, it is reasonable to use χ in the present analysis, too.

In LHD, the recycling neutrals are predominantly ionized in the edge stochastic layer, more than 90% of total recycling flux. It is also estimated the neutral density in the confinement region is on the order of 10^{14} m^{-3} [40]. In this case, the charge exchange time for the 180 keV NBI is estimated as ∼1.5 s. On the other hand, the slowing down time of the beam for the plasma parameters in the present analysis is ∼0.1 s. Since the slowing down time is shorter than the charge exchange time by one order of magnitude, the effects of the neutrals is reasonably negligible.

In the present version of the code, the prompt loss of the fast ions is accounted for by executing orbit tracing, while the neoclassical diffusion of the fast ions is not taken into account. The latter effects is, however, more relevant for the case of low magnetic field ⩽1 T and for perpendicular NBI. (The present analysis focuses on the discharges with high magnetic field, 2.75 T, and the tangential NBI). In the experiments, the NBI deposition power is evaluated by the NB shine-through measurement [29]. The calculated power agrees with the experimental one within the 7.7% standard

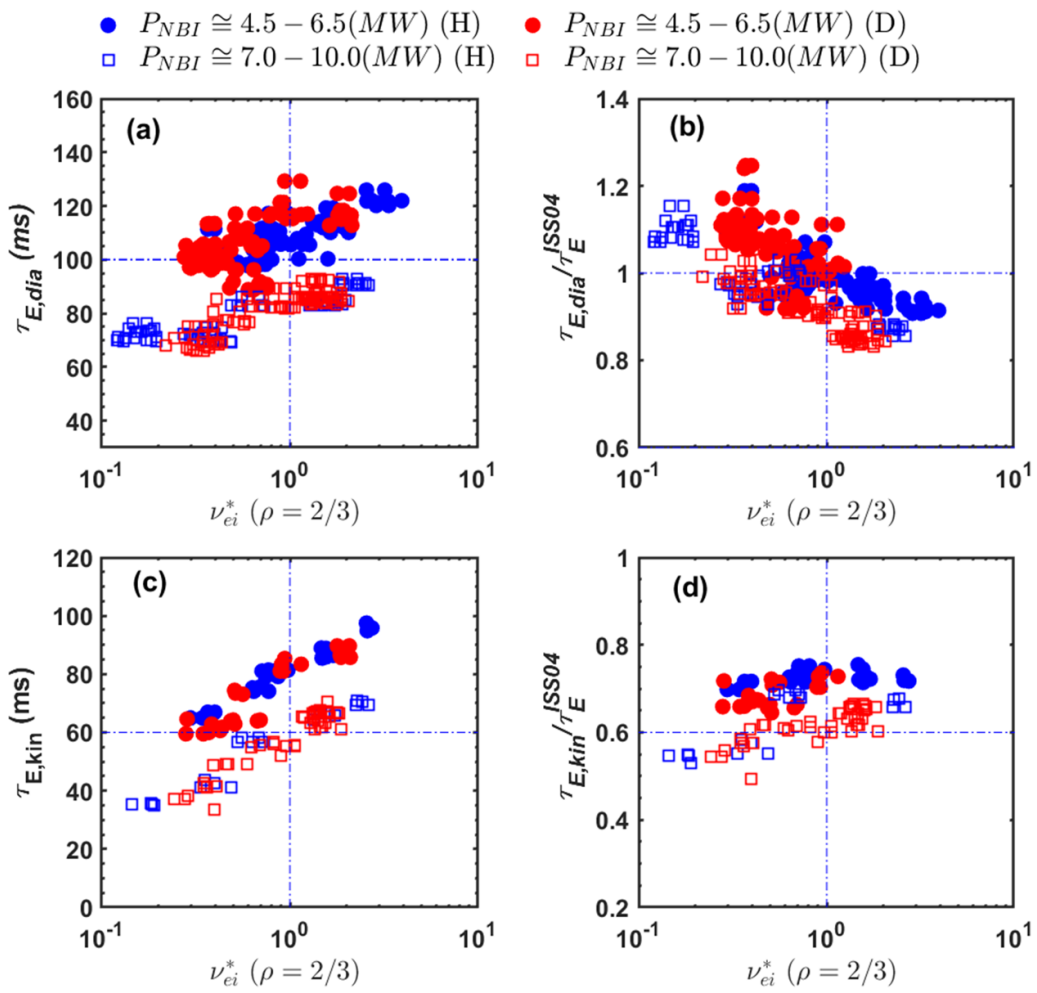

Figure 2. Data points of (*a*), (*b*) $\tau_{E,dia}$, $\tau_{E,dia}/\tau_E^{ISS04}$ and (*c*), (*d*) $\tau_{E,kin}$, $\tau_{E,kin}/\tau_E^{ISS04}$ estimated in H (blue color) and D (red color) dominant plasmas with various NBI deposited heating powers and line-averaged densities as a function of the normalized collisionality measured at $\rho = 2/3$.

deviation. We, therefore, consider that the uncertainty of the NBI absorbed power in the analysis is below 10%.

The n_e, T_e profiles were measured by YAG laser TS and T_i profile was measured by CXRS diagnostics, and we used these profiles as input parameters to calculate the χ_e and χ_i by TASK3D. To incorporate the radial profiles of n_e, T_e and T_i in TASK3D, we have combined two smoothing schemes, such as median filter with seven radial points and average 10–15 radial points. This is because fitting function sometimes largely deviates from the experimental profiles. We have found that the combined smoothing scheme provides most reasonable profiles by removing scatters and spikes in the original data points without large deviation. We calculated the χ_e and χ_i profiles at five nearby time points, where the solid or dashed lines represent average values and the shading is the error range in a standard deviation, as shown in panels (*c*) and (*f*) in figures 3 and 4.

Figures 3(*a*)–(*c*) and (*d*)–(*f*) compare the results between H (blue color) and D (red color) plasmas at low NBI deposited power for low density ($\bar{n}_e \approx 1.5 \times 10^{19}$ m^{-3}) and high density ($\bar{n}_e \approx 4.5 \times 10^{19}$ m^{-3}) discharges, respectively. In figures 4(*a*)–(*c*) and (*d*)–(*f*), the results of the H and D plasmas at high NBI deposited power are compared in a similar fashion for the low and high $\bar{n}_e$ discharges. From these figures, one can see that in low $\bar{n}_e$ discharges the differences in n_e and T_e profiles between the H and D plasmas are much smaller than those in high $\bar{n}_e$ discharges. Figures 3(*a*)–(*c*) and 4(*a*)–(*c*) show that at low $\bar{n}_e$, the n_e and T_e profiles of H plasmas are almost the same as those of the D plasma, only being slightly different, resulting in similar χ_e profiles for H and D isotope gases. In case of high $\bar{n}_e$ discharges, the n_e profiles become much hollower in D plasmas than in H ones, and consequently, T_e profiles are higher in D plasmas. The resultant χ_e profile of H plasmas is slightly higher in the edge ($\rho > 0.6$), while in the inner plasma region ($\rho < 0.6$) it is almost comparable to that of the D ones, as depicted in figures 3(*d*)–(*f*) and 4(*d*)–(*f*). As a result, the total electron energy transport coefficients have similar profiles between H and D dominant plasmas with various $\bar{n}_e$ and P_{NBI}. For the ion temperature, figures 3(*b*), (*e*) and 4(*b*), (*e*) indicate that the T_i profiles between the H and D

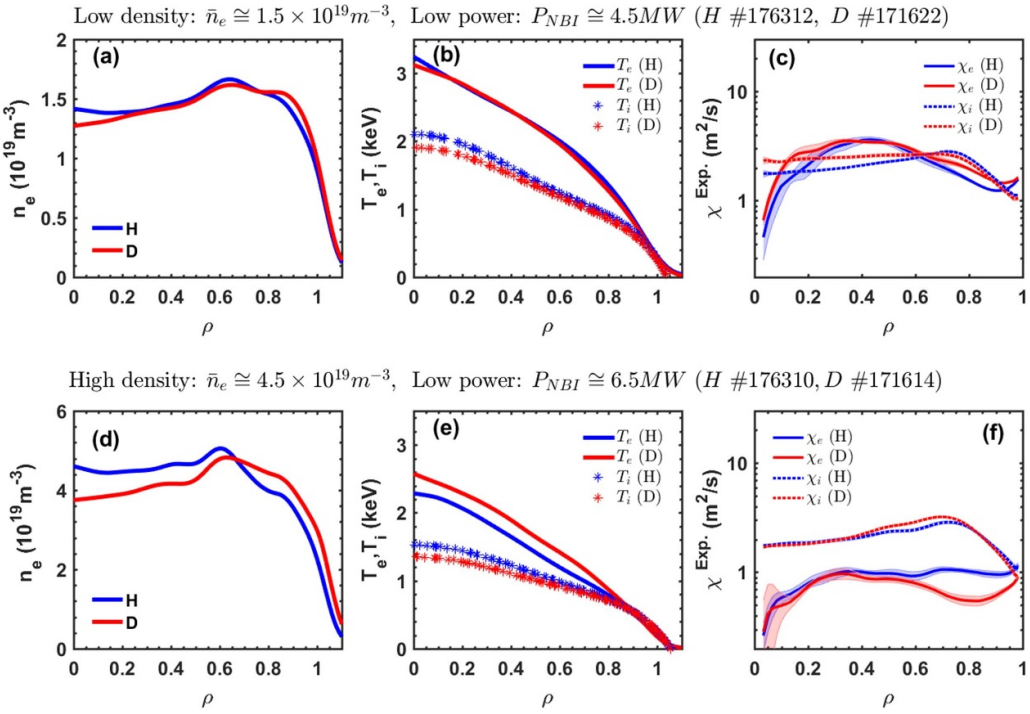

Figure 3. Comparison of radial profiles of n_e, T_e and T_i together with the thermal transport coefficients χ_e and χ_i between H (blue color) and D (red color) plasmas in low NBI heating power for (*a*)–(*c*) low density ($\bar{n}_e \approx 1.5 \times 10^{19}$ m^{-3}) and (*d*)–(*f*) high density ($\bar{n}_e \approx 4.5 \times 10^{19}$ m^{-3}).

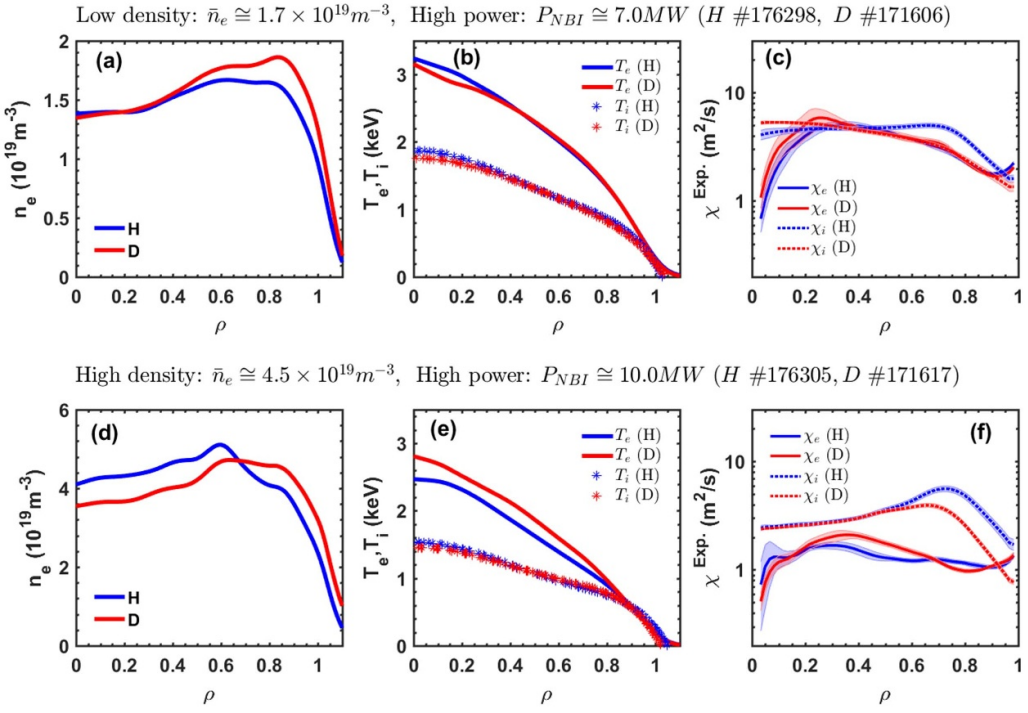

Figure 4. Comparison of radial profiles of n_e, T_e and T_i together with the thermal transport coefficients χ_e and χ_i between H (blue color) and D (red color) plasmas in high NBI heating power for (*a*)–(*c*) low density ($\bar{n}_e \approx 1.7 \times 10^{19}$ m^{-3}) and (*d*)–(*f*) high density ($\bar{n}_e \approx 4.5 \times 10^{19}$ m^{-3}).

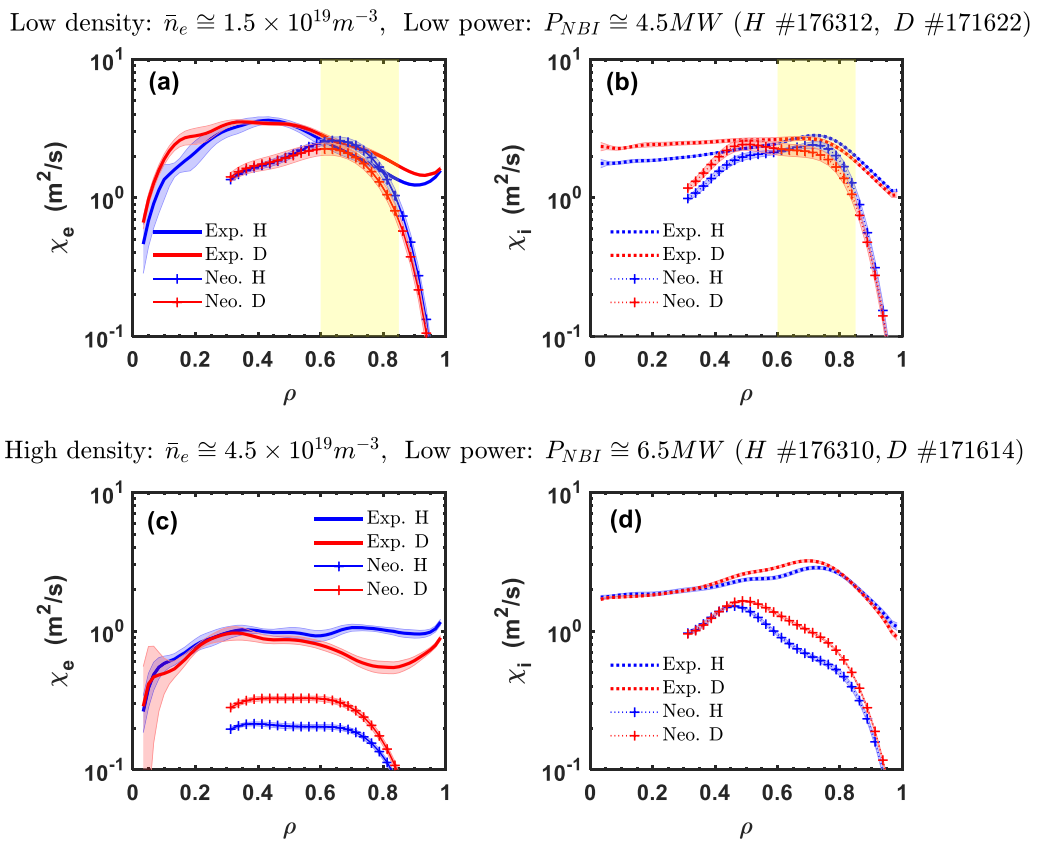

Figure 5. Comparison of radial profiles of the experimental (Exp.) and the neoclassical (Neo.) thermal transport coefficients between H (blue color) and D (red color) plasmas in low NBI heating power for (*a*), (*b*) low density ($\bar{n}_e \approx 1.5 \times 10^{19}$ m^{-3}) and (*c*), (*d*) high density ($\bar{n}_e \approx 4.5 \times 10^{19}$ m^{-3}).

plasmas are always analogous once they have nearly equivalent deposited power and line-averaged density. Therefore, in all discharges the χ_i profiles of H and D plasmas are generally similar despite minor distinction. Above results are different from those observed in the ECRH discharges, in which the isotope effects are reflected mainly on ion energy transport [13], while for the NBI heating the isotope effects has no obvious influence on both ion and electron energy transport.

To gain an insight into the contribution of the neoclassical transport to the experimentally obtained total energy transport in the H and D majority plasmas, figures 5 and 6 illustrate the calculated experimental (Exp.) and neoclassical (Neo.) thermal transport coefficients in both H and D plasmas at low ($P_{\rm NBI} \approx$ 4.5–6.5 MW) and high ($P_{\rm NBI} \approx$ 7.0–10.0 MW) NBI heating deposited powers, respectively. Here, the neoclassical values of χ_e and χ_i were calculated by the numerical code GSRAKE [41] and used same density and temperature profiles as in the TASK3D as input parameters for calculating the neoclassical values. The experimental thermal transport coefficient, in principle, represents a summation of the neoclassical and turbulent transport, i.e. $\chi^{Exp.} = \chi^{Neo.} + \chi^{Tur.}$ [42]. In figure 5, the χ_e and χ_i profiles in H (blue curves) and D (red curves) dominant plasmas with low $P_{\rm NBI}$ are plotted in the top panels for low density discharges ($\bar{n}_e \approx 1.5 \times 10^{19}$ m^{-3}) and in the bottom panels for high density discharges ($\bar{n}_e \approx 4.5 \times 10^{19}$ m^{-3}). Figures 6(*a*)–(*d*) depict the χ_e and χ_i profiles of H and D plasmas at high P_{NBI} for low $\bar{n}_e$ discharges ($\bar{n}_e \approx 1.7 \times 10^{19}$ m^{-3}) and high $\bar{n}_e$ discharges ($\bar{n}_e \approx 4.5 \times 10^{19}$ m^{-3}), respectively. In figures 5 and 6, the calculated neoclassical transport coefficients show quite clear difference of the isotope effects between low and high $\bar{n}_e$ discharges. In low $\bar{n}_e$ case the neoclassical χ_e and χ_i values are nearly equal between H and D dominant plasmas, while in high $\bar{n}_e$ case the neoclassical χ_e and χ_i in H plasmas are lower than in D ones. The contribution of the neoclassical transport to the total thermal transport also exhibits different features between low and high $\bar{n}_e$ discharges. For both H and D plasmas, in low $\bar{n}_e$ shots the neoclassical χ_e and χ_i are comparable to the experimental transport coefficients at $\rho \approx 0.6 - 0.85$ (see yellow shades) and less than experimental transport coefficients in the core ($\rho < 0.6$) and edge ($\rho > 0.85$) regions, whereas in high $\bar{n}_e$ shots the neoclassical χ_e and χ_i are overall lower than the experimentally measured transport coefficients. These results illustrate that in low $\bar{n}_e$ of both H- and D-dominant plasmas, electron and ion thermal transport are dominated by neoclassical transport at a certain zone ($\rho \approx 0.6 - 0.85$), while the anomalous transport process has the primary effect in the remaining area. Besides, in both H- and D-dominant plasmas, with increase of $\bar{n}_e$ the reduction of neoclassical energy transport is more significant than the reduction of total transport, and hence, the turbulent transport becomes prevailing at high $\bar{n}_e$. This feature is clearly different from that observed in

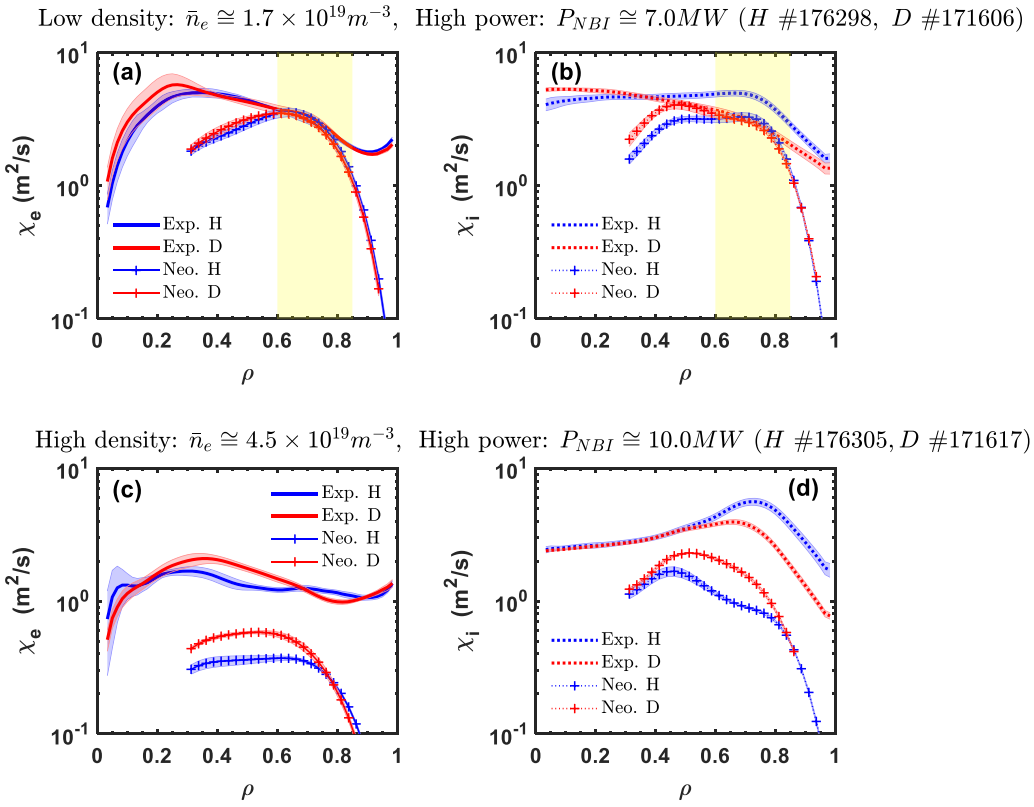

Figure 6. Comparison of radial profiles of the experimental (Exp.) and the neoclassical (Neo.) thermal transport coefficients between H (blue color) and D (red color) plasmas in high NBI heating power for (*a*), (*b*) low density ($\bar{n}_e \approx 1.7 \times 10^{19}$ m^{-3}) and (*c*), (*d*) high density ($\bar{n}_e \approx 4.5 \times 10^{19}$ m^{-3}).

ECRH plasmas at LHD, in which the turbulent transport prevails in low density discharges [13].

In figures 5 and 6, it is noticed that in both low and high NBI heating cases, with increasing $\bar{n}_e$ the experimental χ_e values drop remarkably, while the variation in χ_i values is quite small for both H and D majority plasmas. Figure 7 plots the radial profiles of experimental (figures 7(*a*)–(*d*)) and neoclassical (figures 7(*e*)–(*h*)) transport coefficients in different $\bar{n}_e$ of H and D discharges with low/high P_{NBI}. It is clearly seen that for both H and D plasmas, the χ_e values generally decrease with increasing $\bar{n}_e$ and the decrease in ${\chi_e}^{neo.}$ is more significant than ${\chi_e}^{Exp.}$, which indicates that in NBI discharges the anomalous transport process has the main effect in high density $\bar{n}_e$. Meanwhile, figures 8(*a*) and (*b*) further summarize the χ_e and χ_i values in H- and D-discharges as a function of the ratio of NBI deposited heating powers on electron (P_e) and ion (P_i) to line-averaged densities. For electrons, both ${\chi_e}^{Exp.}$ and ${\chi_e}^{neo.}$ decrease with increasing density (decreasing $P_e/\bar{n}_e$). The tendency is similar to that observed in ECR heated plasmas [13], where the χ_e values reduce with the increase of collitionality ($\nu_h^* \propto \bar{n}_e$). However, the influence of $\bar{n}_e$ on χ_i seems to be different between the ECR and NBI heated plasmas. In [13], it is shown that with ECRH the χ_i increases with increasing ν_h^*, whereas in our case the χ_i appears to be unchanged or even decreased with increasing $\bar{n}_e$ by the NBI heating, as shown in figure 8(*b*). The results suggest an importance of heating scheme on the ion energy transport, while the electron energy transport is not affected very much. The underlying physics of the phenomena needs to be further studied for prediction of energy transport in future reactors where the heating processes will be different from those in the present-day devices due to the alpha particle heating.

3.2. Comparison of turbulence characteristics between isotopic H- and D-dominant plasmas

3.2.1. Turbulence characteristics in core plasmas. As turbulent energy transport plays a quite important role in the present NBI-heated H and D discharges, it is necessary to compare further the characteristics of turbulence between isotopic H- and D-dominant plasmas. To this end, we have investigated the turbulence properties in H and D plasmas at low and high $\bar{n}_e$ discharges using the 2D PCI diagnostic. Figure 9 depicts the results in low density discharges ($\bar{n}_e \approx 1.7 \times 10^{19}$ m^{-3}) with same NBI deposited power for H and D in the left and right column, respectively. Figures 9(*a*-1), (*a*-2) and (*b*-1), (*b*-2) show that the equilibrium density and electron/ion temperatures all have similar radial dependences between H and D dominant plasmas. The radial profiles of density fluctuations exhibit slightly smaller amplitude in H plasmas, as shown in

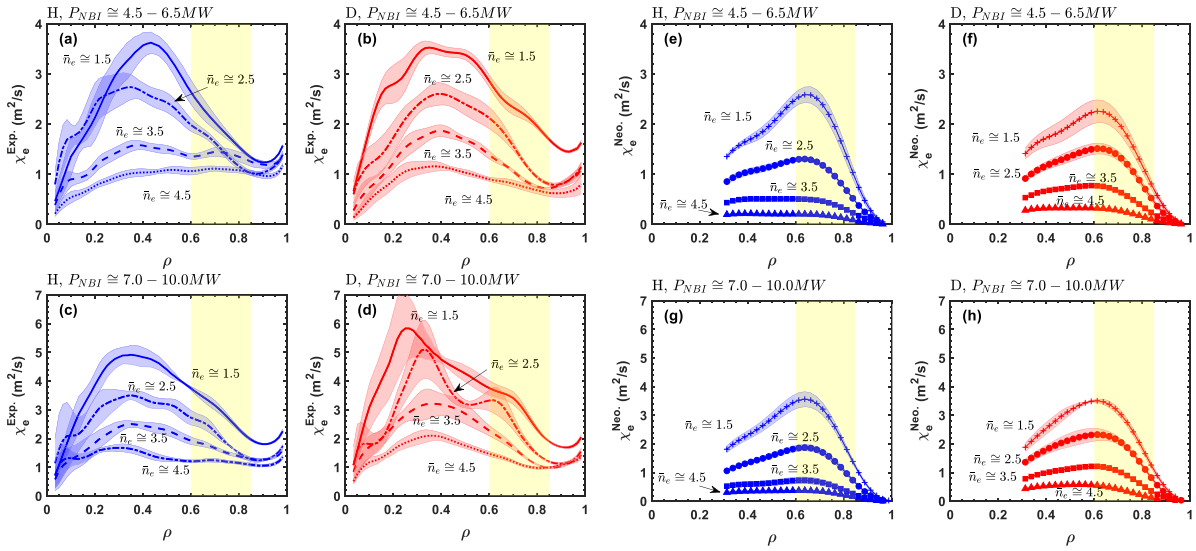

Figure 7. Radial profiles of (*a*)–(*d*) the experimental (Exp.) and (*e*)–(*h*) the neoclassical (Neo.) electron thermal transport coefficients χ_e in different $\bar{n}_e$ of H (blue color) and D (red color) plasmas. Top (bottom) panels are low (high) P_{NBI} discharges.

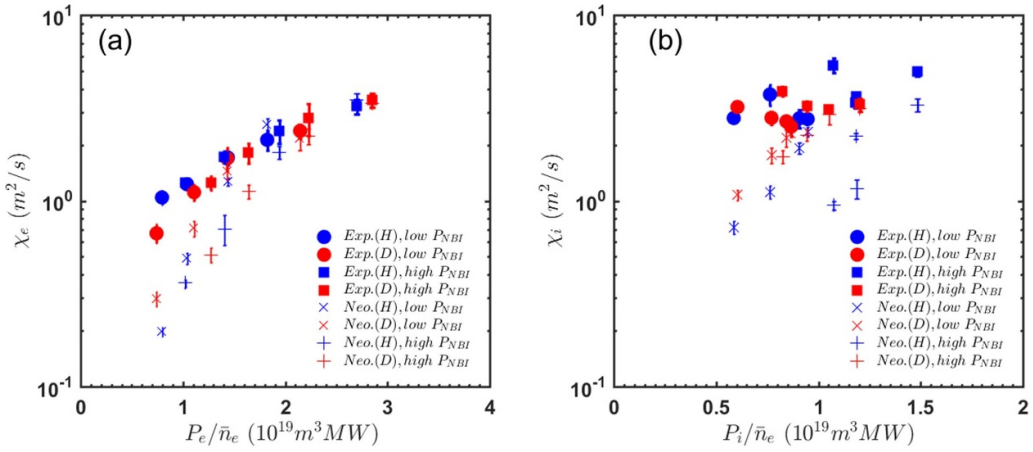

Figure 8. Data points of (*a*) χ_e and (*b*) χ_i in H (blue color) and D (red color) discharges with various ratios of NBI deposited heating powers on electrons (P_e) and ions (P_i) to line-averaged densities.

figures 9(*a*-3) and (*b*-3). The bottom two panels show radial distributions of the *k* spectrum (mainly along the poloidal direction) and phase velocity of density fluctuations. As seen in 9(*a*-4), (*a*-5) and (*b*-4), (*b*-5), turbulence in both H and D cases propagates along the ion diamagnetic drift direction ($\omega_{*,i}$) in the laboratory frame. The $E_r \times B_t$ drift velocity can be roughly estimated by the Doppler shift, as overplotted by the black curves in figures 9(*a*-5) and (*b*-5). Since the Doppler shift is in the electron diamagnetic drift ($\omega_{*,e}$) direction in both cases, it is thought that in the plasma rest frame the fluctuations also propagate along the $\omega_{*,i}$ direction, suggesting a nature of an ion mode. The local scale of the turbulence mode is estimated to be $k\rho_i \approx 0.4-0.7$ at the position $\rho \approx \pm(0.7$–$0.9)$. It is therefore considered that the turbulence is driven by the ITG in both H and D discharges at low densities. In the case of low NBI heating discharges, the turbulence exhibits similar characteristics in both H and D plasmas to those in high NBI heating discharges.

In high density ($\bar{n}_e \approx 4.5 \times 10^{19}m^{-3}$) discharges, the turbulence properties in H and D plasmas with same NBI deposited power are illustrated in figure 10. The equilibrium density and electron/ion temperature profiles show slight differences between the H and D plasmas, as displayed in figures 10(*a*-1), (*a*-2) and (*b*-1), (*b*-2). Meanwhile, the radial profiles of density fluctuations also exhibit slight discrepancy between the H and D plasmas, as plotted in figures 10(*a*-3) and (*b*-3). For density fluctuation propagations, the bottom two panels of the *k* spectrum and the phase velocity indicate that in both H and D cases turbulence propagates along $\omega_{*,e}$ direction in the laboratory frame, opposite to those in low $\bar{n}_e$ discharges. Since the Doppler $E_r \times B_t$ shift is also in the $\omega_{*,e}$ direction and this value is almost comparable to the turbulence phase velocity, from these observations the turbulence propagation direction in the plasma frame and nature of mode are uncertain. In addition, using the density and electron/ion temperature profile data shown in figures 9 and 10, we have computed the η_e and η_i

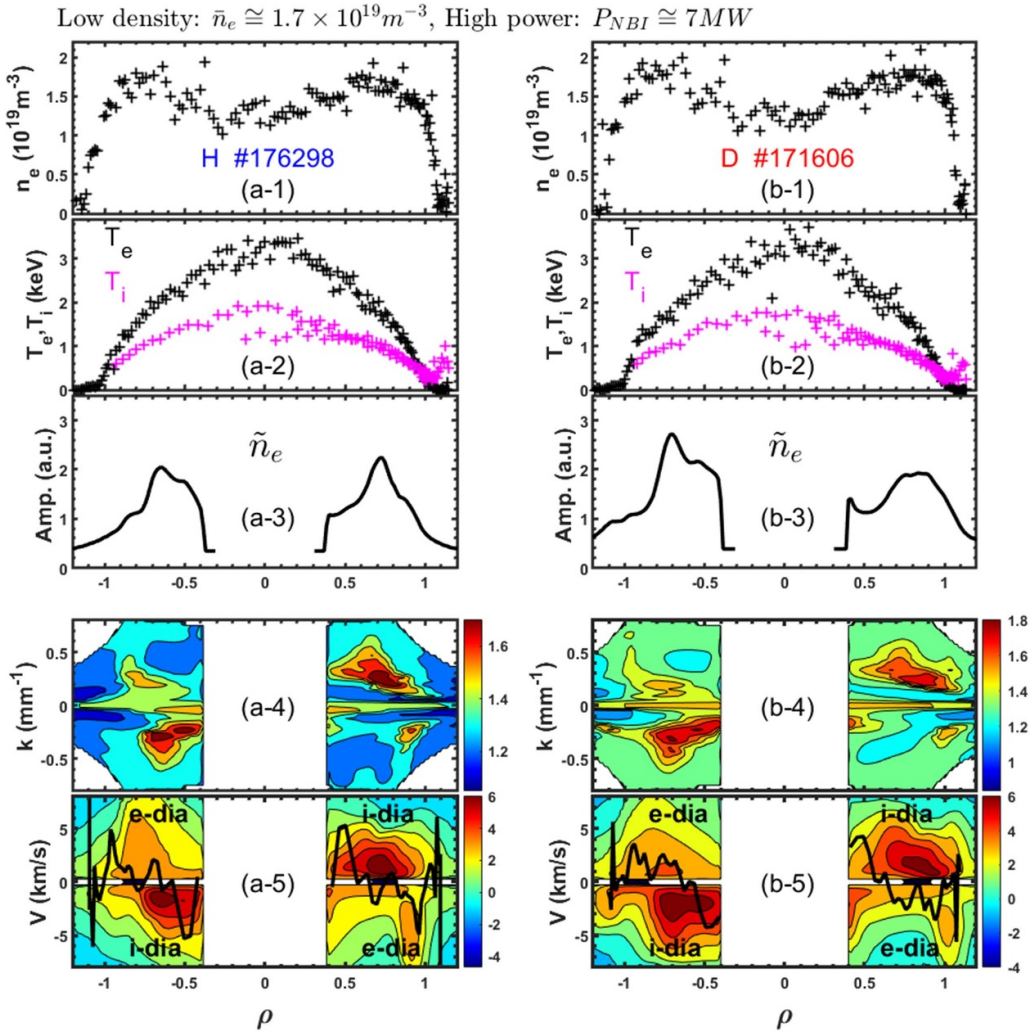

Figure 9. Radial profiles of n_e, T_e and T_i, the amplitude of density fluctuation ($\tilde{n}_e$), the k spectrum and the phase velocity of $\tilde{n}_e$ in low density ($\bar{n}_e \approx 1.7 \times 10^{19} m^{-3}$) H (left column) and D (right column) discharges. In (a-5) and (b-5), the black curves represent the $E_r \times B_t$ poloidal rotation velocities measured by CXRS.

values in both low- and high-density discharges of H and D plasmas. The results show that in all scenarios the η_e and η_i values are larger than 1, which means that these values conform to the theoretical prediction thresholds for electron and ion thermal transport driven by TEM and ITG modes, e.g. the $\eta_e \equiv \partial_r \ln T_e / \partial_r \ln n > 1$ for the TEM and $\eta_i \equiv \partial_r \ln T_i / \partial_r \ln n > 1$ for the ITG, respectively [43]. Consequently, the nature of mode at high $\bar{n}_e$ case is unclear. Numerical simulations are demanded to study further on this issue.

It is noticed that in the NBI heated plasmas, with increasing $\bar{n}_e$ the density fluctuation levels are enhanced in both H and D discharges (see figures 9 and 10), consistent with the results estimated in figures 5 and 6, i.e. the turbulent energy transport prevails in high density discharges. With regard to the isotope effects, in high $\bar{n}_e$ discharges (i) the experimentally observed lower density fluctuation levels in D plasmas (see figure 10) agree fairly with lower $\chi^{Tur.}$ values ($\chi^{Tur.} = \chi^{Exp.} - \chi^{Neo.}$) calculated by the simulation codes (see figures 5 and 6); (ii) different density fluctuation amplitudes (or turbulent transport) between H and D dominant plasmas may be compensated by the neoclassical transport so that the total confinement is nearly at the same level for H and D plasmas. These results are different from those measured in the ECR heated low $\bar{n}_e$ discharges at LHD, where higher density fluctuation amplitudes in D discharges cannot account for better energy confinement in the D plasma [13]. Besides, the turbulence characteristics with NBI heating also manifest several other distinct features compared to ECRH plasmas [13]. For high density cases, the turbulence propagates in different directions between H and D plasmas, and H plasma has a wider unstable region in ECRH. But, for high $\bar{n}_e$ in NBI heating, the fluctuations of both H and D plasmas propagate along the $\omega_{*,e}$ direction and the unstable spatial region are also similar.

3.2.2. Turbulence characteristics in the edge region. In order to gain an insight into the isotopic effects on edge turbulence, the three-wave nonlinear interaction among edge density fluctuations ($\tilde{n}_e$) measured by the reflectometer in H and D plasmas has been analyzed using the bispectral analysis

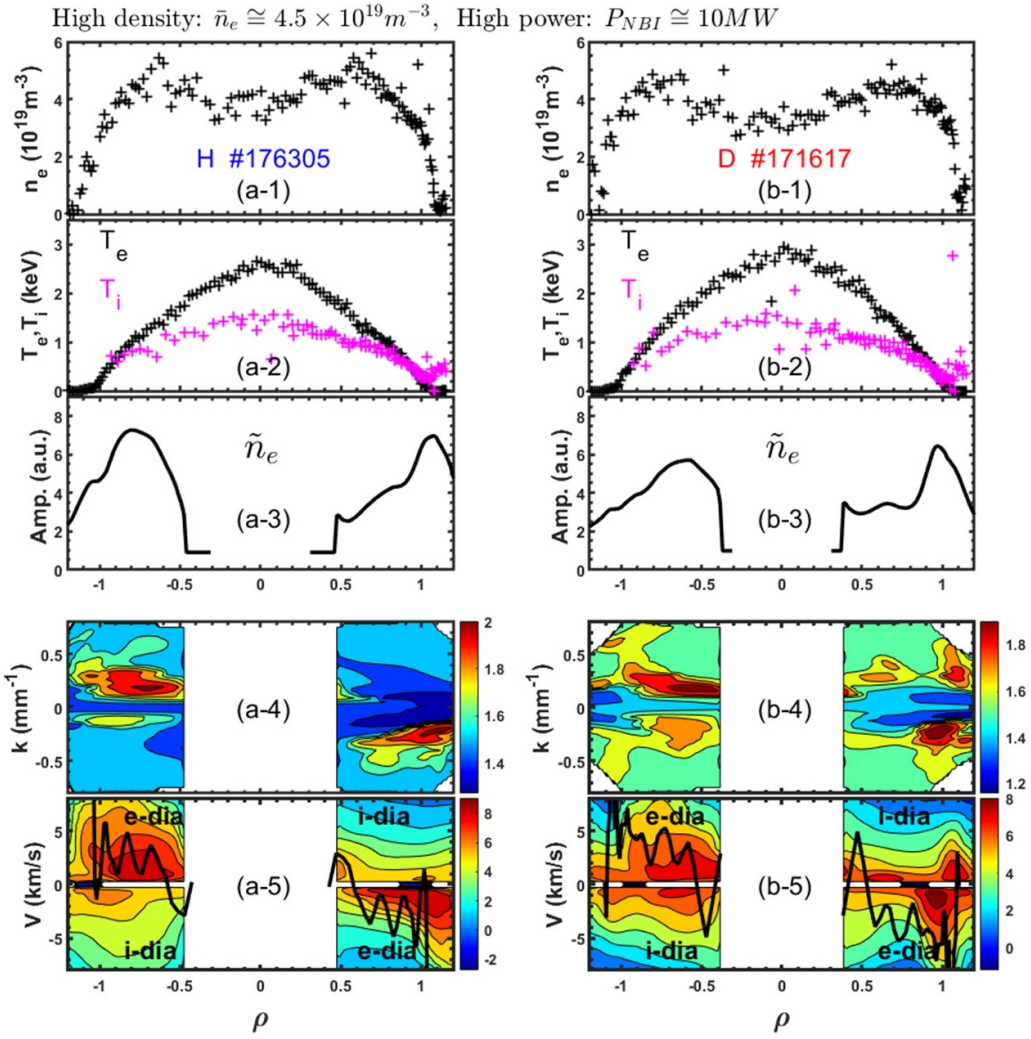

Figure 10. Radial profiles of n_e, T_e and T_i, the amplitude of density fluctuation ($\tilde{n}_e$), the k spectrum and the phase velocity of $\tilde{n}_e$ in high density ($\bar{n}_e \approx 4.5\times10^{19}$ m^{-3}) H (left column) and D (right column) discharges. In (a-5) and (b-5), the black curves represent the $E_r \times B_t$ poloidal rotation velocities measured by CXRS.

technique [44, 45]. The bispectrum is defined as $b_{XYZ}(f_1,f_2) = X(f_1)\,Y(f_2)\,Z^*(f_1+f_2)$ and the normalized squared bicoherence is ${B_{XYZ}}^2(f_1,f_2) = {b_{XYZ}}^2/\langle|X(f_1)\,Y(f_2)|^2\rangle\langle|Z^*(f_1+f_2)|^2\rangle$. The ${B_{XYZ}}^2$ represents the degree of three-wave coupling at frequencies f_1, f_2 and f, where the $X(f)$, $Y(f)$ and $Z(f)$ are the Fourier transform of fluctuation signals $x(t)$, $y(t)$ and $z(t)$, respectively. In this study, we have analyzed the auto-bispectrum of density fluctuations, i.e. $x(t)$= $y(t)$= $z(t)$= $\tilde{n}_e$ (t). The summed squared bicoherence $\sum B^2(f) = \sum_{f=f_1+f_2} B^2(f_1,f_2)/N(f)$ has also been computed to understand the bicoherence for all frequencies obeying the selection rule $f = f_1 + f_2$, where $N(f)$ is the number of Fourier components for each f in the summation.

Figures 11 and 12 show the auto-bicoherence spectra of edge density fluctuations in H/D plasmas in low $\bar{n}_e$ and high $\bar{n}_e$ cases, respectively. As depicted in figure 11(a), the x-axis, y-axis and color bar represent the frequencies f_1 and f_2 and the relative strength of nonlinear coupling in H plasma. It is clear that the bicoherence value at $f = f_1 + f_2 \approx 5$ kHz or $f_2 = \pm5$ kHz is much higher than those at other frequencies. A distinct peak at $f \sim 5$ kHz is also found on the summed squared bicoherence $\sum B^2(f)$, as shown in figure 11(b). These results suggest that there is a significant three wave interaction in edge density fluctuations of low-density H plasmas. Similarly, the bispectral analysis has also been applied to D dominant plasmas. The results are plotted in figures 11(c) and (d). One can see that the three-wave coupling also exists in D plasmas, but the coupling intensity is much weaker than that in H ones, as evidenced also in figures 11(b) and (d), where the value of $\sum B^2(f)$ in H plasmas is much higher than that in D ones. In case of high density discharges, the nonlinear interaction of edge turbulence turns to be weaker in both H and D majority plasmas, as illustrated in figure 12. The contour plot of bicoherence becomes less sharp in the H discharge (see figure 12(a)) and the bicoherence almost disappears in the D discharge (see figure 12(c)). The impact of increasing density on damping the three-wave interaction of turbulence has also been observed earlier in TEXTOR [45]. Nevertheless, in the high density discharges the bicoherence of edge density fluctuations remain stronger in H plasmas than that in D ones. The

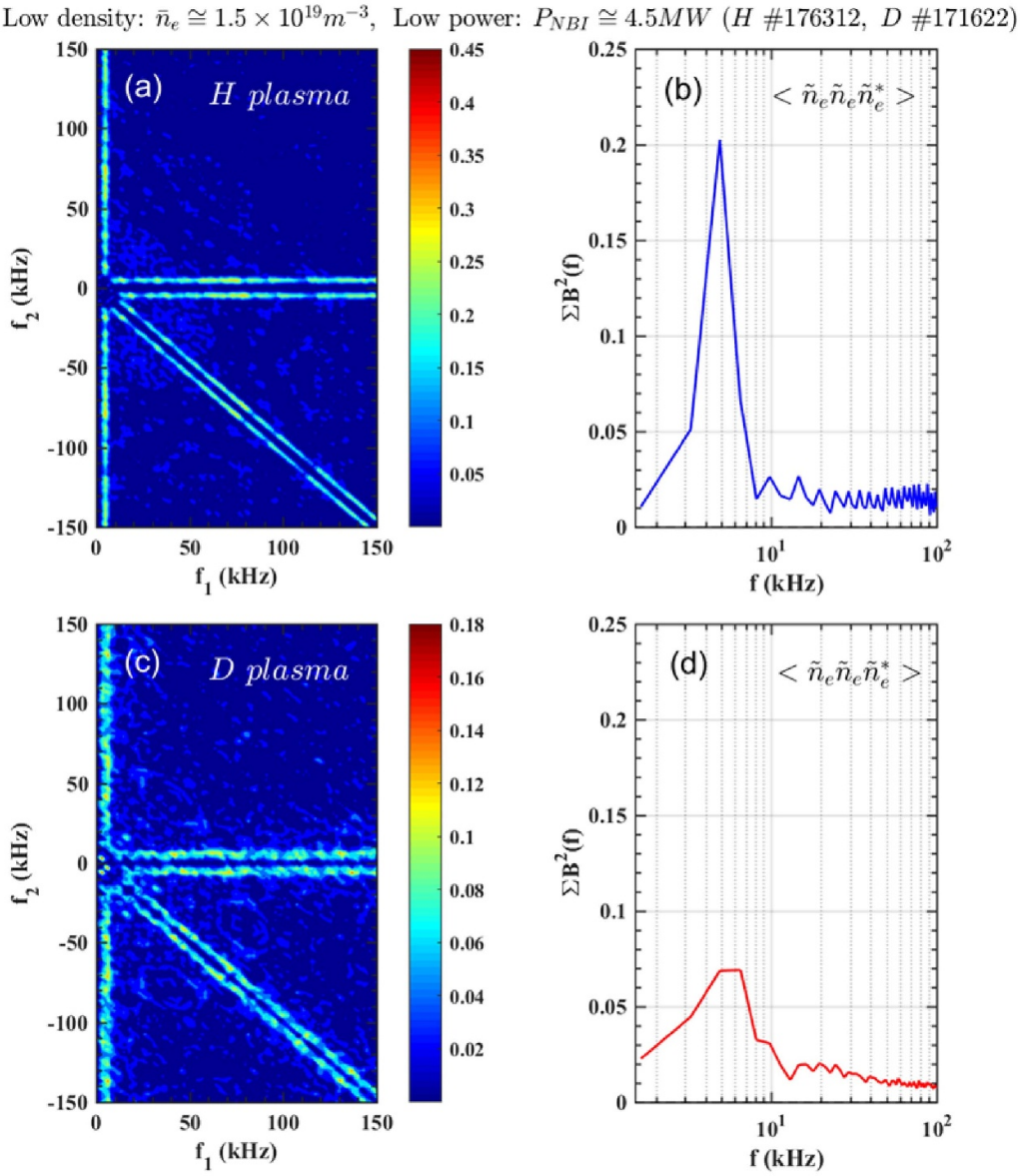

Figure 11. Bispectral analysis of density fluctuations measured at $\rho \sim 0.95$ in the H plasma (top) and at $\rho \sim 0.99$ in the D plasma (bottom) of the low density discharge. (*a*), (*c*) Bicoherence $B^2(f_1,f_2)$ and (*b*), (*d*) the summed squared bicoherence $\sum B^2(f)$. The color bar represents the intensity of the squared bicoherence.

above results reveal that in the NBI heated plasmas at LHD there exist clear isotopic effects on edge turbulence, i.e. the nonlinear coupling of edge turbulence is much stronger in H plasmas.

To understand underlying mechanisms for the difference on the turbulence nonlinear coupling between H and D plasmas, we have explored possible reasons responsible for the nonlinear interaction of turbulence, i.e. energy cascading from small-scale turbulence eddies to large-scale zonal flows. According to the theory [46–48], the generation of zonal flows can be attributed to the radial gradient of Reynolds stress together with its damping rate, i.e. $\frac{\partial V_\theta}{\partial t} = \frac{\partial}{\partial r}\langle \tilde{V}_r \tilde{V}_\theta \rangle - \gamma_{\rm damp} V_\theta$, where V_θ, $\langle \tilde{V}_r \tilde{V}_\theta \rangle$ and $\gamma_{\rm damp}$ denote the zonal flow, Reynolds stress and the flow damping rate, respectively. From figures 9 and 10, it is seen that the density fluctuation amplitudes between H and D plasmas are comparable in low density cases and it is slightly lower for D in high density discharges. Thus, it is assumed that the driving term of the Reynolds stress induced by fluctuating velocities imposes similar effects on H and D plasmas, ignoring the phase influence between $\tilde{V}_r$ and $\tilde{V}_\theta$ fluctuations. As a consequence, the difference on the zonal flow generation may arise from different damping rates between H and D plasmas. To this end, we have compared the radial profiles of edge n_e, T_e in figure 13. The results clearly show that in the edge region the D plasma has higher density (n_e) and slightly lower temperature (T_e), leading to higher damping rate for zonal flows ($\gamma_{\rm damp} \propto n_e/T_e^{3/2}$). This might explain why the H plasma has stronger nonlinear coupling than that in the D plasma.

The above results indicate that for the NBI heated plasmas in LHD there is a clear difference in turbulence characteristics

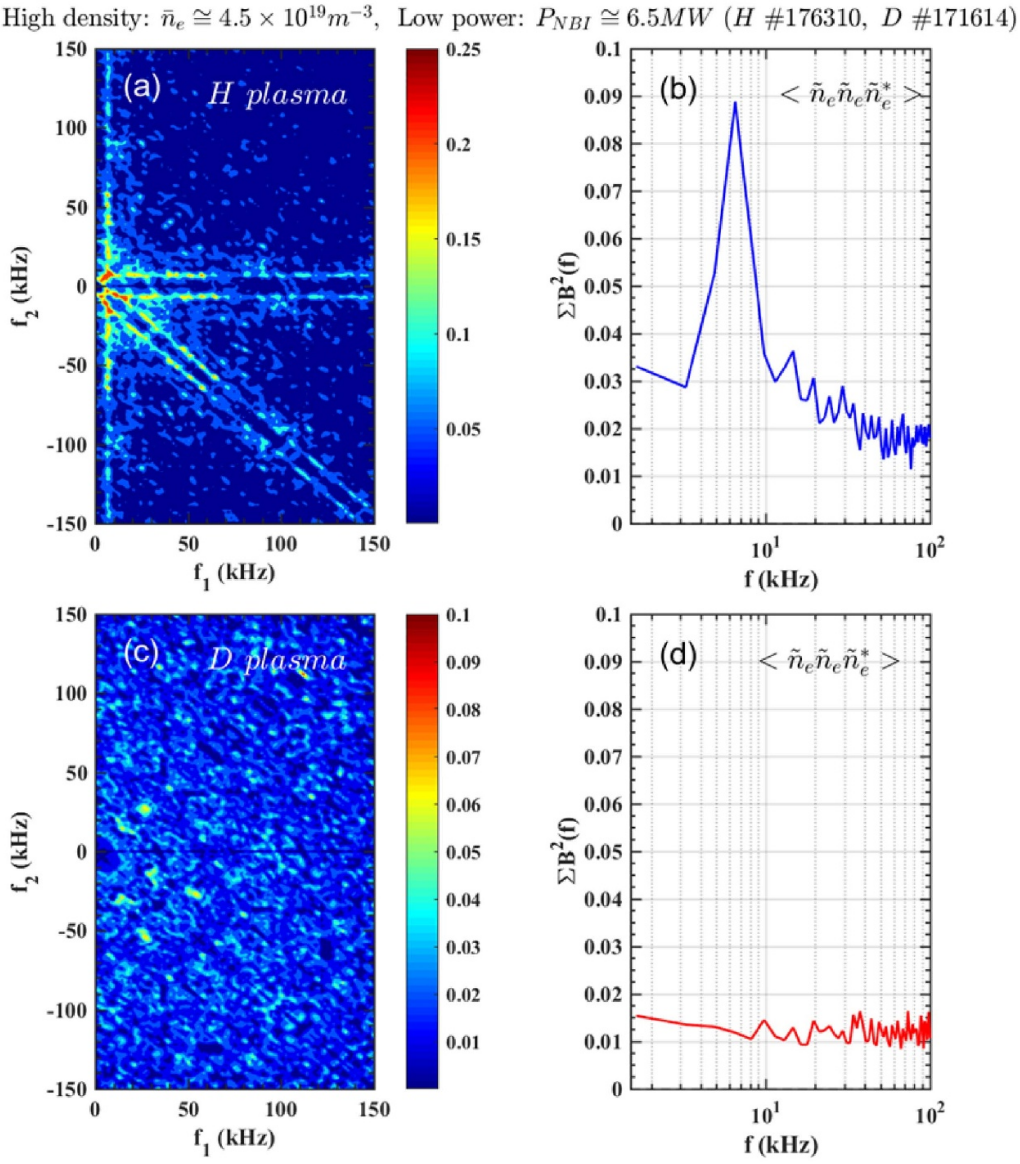

Figure 12. Bispectral analysis of density fluctuations measured at $\rho \sim 1.06$ in the H plasma (top) and at $\rho \sim 1.05$ in the D plasma (bottom) of the high density discharge. (*a*), (*c*) Bicoherence $B^2(f_1,f_2)$ and (*b*), (*d*) the summed squared bicoherence $\sum B^2(f)$. The color bar represents the intensity of the squared bicoherence.

between core and edge regions, that is, the isotope effects are more pronounced in the edge region than in the core region, whereas the global confinement is not affected by the difference in the edge. The discrepancy in the edge turbulence characteristics for H and D plasmas would play more significant roles in the plasma-wall interaction, such as broadening of divertor heat flux channel [49], which is also a critical issue for future reactors.

4. Summary

In this study, we report the experimental results of the isotope effects on the plasma confinement, transport and fluctuation characteristics in H- and D-dominant plasmas at LHD with similar operational parameters, such as the heating power, magnetic field, electron/ion temperature and line-averaged density. Results show that under similar discharge conditions (i) the global energy confinement has no significant dependence on the isotope mass, $\tau_E(H) \approx \tau_E(D)$; (ii) both of electron and ion total energy transport, the total transport coefficients have similar profiles between H and D dominant plasmas. In low $\bar{n}_e$ cases the neoclassical χ_e and χ_i values are nearly equal between H and D dominant plasmas, while in high $\bar{n}_e$ cases the neoclassical χ_e and χ_i in H plasmas are lower than in D ones; (iii) in low $\bar{n}_e$ of both H- and D-dominant plasmas, electron and ion thermal transport are dominated by neoclassical transport at a certain zone ($\rho \approx 0.6$–0.85), while the anomalous transport process has the primary effect in the remaining area. In high $\bar{n}_e$ discharges, turbulent transport prevails at all radial positions for both H and D plasmas; (iv) in low $\bar{n}_e$ shots, density fluctuations exhibit ITG nature. In case of high $\bar{n}_e$, density fluctuations propagate in the $\omega_{*,e}$ direction with slightly

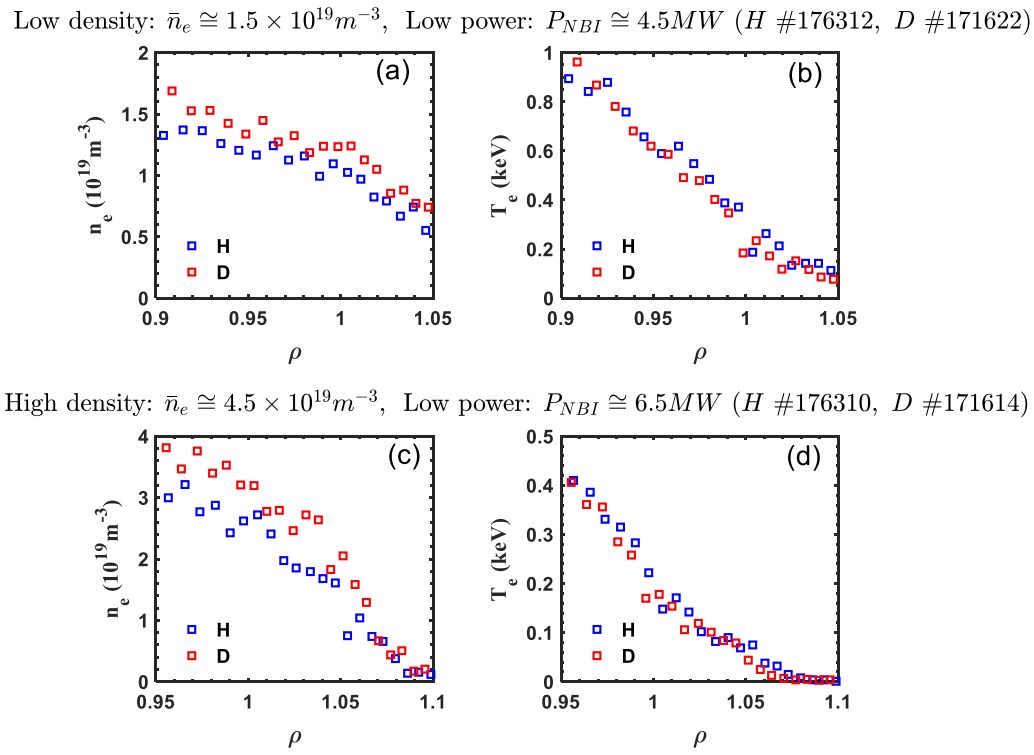

Figure 13. Comparison of radial profiles of edge n_e and T_e between H (blue color) and D (red color) plasmas for (*a*), (*b*) low density ($\bar{n}_e \approx 1.5 \times 10^{19}\mathrm{m}^{-3}$) and (*c*), (*d*) high density ($\bar{n}_e \approx 4.5 \times 10^{19}\mathrm{m}^{-3}$) discharges.

larger amplitude in H plasmas, while the turbulence mode is unclear in the present analysis; (v) there exists stronger nonlinear coupling in edge density fluctuations in H plasmas for both low and high density cases than that in D ones, due to probably lower damping rate for the nonlinear three wave interaction in H plasmas. The isotope effects on the turbulence characteristics is more pronounced in the edge region than in the core region, although the global confinement is not essentially affected.

In the gyrokinetic simulations performed by Nakata *et al* [23], the isotope effects on turbulence and zonal flows in helical plasmas have been addressed. Here, a brief qualitative comparison between the simulation results and our experimental observations is appropriate. In [23], it is shown that combined effects of the collisional TEM stabilization by heavier isotope ions and the increased impact of stronger zonal flows in heavier isotope plasmas lead to the significant transport reduction with the isotope mass dependence opposite to the gyro-Bohm scaling. For the linear ITG and collisionless linear TEM turbulence, the heat diffusivity ($\chi_s \propto \gamma/k_\perp^2$) exhibits gyro-Bohm mass dependence, i.e. $\gamma/k_\perp^2 \propto \sqrt{A_i}$. For collisional linear and also the nonlinear TEM, the heat diffusivity decreases with increased isotope mass. Meanwhile, the nonlinear zonal flow in D plasmas is stronger than in H ones. In our experiments, while the ITG turbulence plays a dominant role in low density discharges, the nature of TEM turbulence cannot be well identified in high density shots. The experimental results indicate that in low $\bar{n}_e$ discharges the turbulent transport coefficients of χ_e and χ_i are both nearly equal between H and D dominant plasmas, whereas in high $\bar{n}_e$ discharges (relatively higher collisionality) the turbulent χ_e and χ_i in D plasmas are lower than those in H ones. Moreover, the isotope effect on turbulence characteristics at LHD is more pronounced in the edge than in the core region, although the global confinement is not essentially different. At the plasma edge, there exists stronger nonlinear coupling (i.e. zonal flows) in density fluctuations in H plasmas for both low and high density cases than that in D ones.

Although the isotope effects on turbulent transport in high density plasmas at LHD appear to be consistent with the simulation work, the global confinement is not affected. And also, the other experimental results are mostly not in accordance with the simulation ones obtained in [23]. It is also noted that the resistive interchange mode might play a role at the collisional regime. In this sense, more sophisticated theoretical and simulation work would be very helpful.

In addition, for deepening our understanding on the isotope effects, we have also compared the present results with those observed in the ECRH discharges at LHD [13]. The main contrasts are listed in table 1. The reasons for the similarities and dissimilarities between these two different heating methods are not clear yet. To unravel the underlying physics, input from theories and simulations is necessary. At present, our findings is limited to the range of the percentage of each majority species, while we have obtained substantial understanding of the isotope effects as discussed above. Experiments and analysis with purer hydrogen isotope plasmas are left for future works.

Table 1. Comparison of energy confinement time, equilibrium profiles, energy transport coefficients, transport mechanisms and turbulence ($\tilde{n}_e$) properties between ECRH [13] and NBI (present experiment) plasmas at LHD.

Heating scheme			ECRH [13]	NBI (present experiment)
Energy confinement time (τ_E)			$\tau_E(H) < \tau_E(D)$	$\tau_E(H) \approx \tau_E(D)$
Equilibrium profiles	n_e		Hollower in D than in H	
	T_e	Low $\bar{n}_e$	$T_e(H) \approx T_e(D)$	
		High $\bar{n}_e$	$T_e(H) < T_e(D)$	
	T_i		$T_i(H) \approx T_i(D)$	$T_i(H) \geqslant T_i(D)$
Energy transport coefficients	χ_e		$\chi_e(H) = \chi_e(D)$	$\chi_e^{Exp.}(\mathrm{H}) \approx \chi_e^{Exp.}(\mathrm{D})$ $\chi_e^{Neo.}(\mathrm{H}) \leqslant \chi_e^{Neo.}(\mathrm{D})$
	χ_i		$\chi_i(H) > \chi_i(D)$	$\chi_i^{Exp.}(\mathrm{H}) \approx \chi_i^{Exp.}(\mathrm{D})$ $\chi_i^{Neo.}(\mathrm{H}) \leqslant \chi_i^{Neo.}(\mathrm{D})$
Transport mechanisms		Low $\bar{n}_e$	Turbulence dominant	Neoclassical dominant in ρ =0.6–0.85, turbulence dominant in rest area
		High $\bar{n}_e$	Neoclassical dominant in ρ =0.6–0.85, turbulence dominant in rest area	Turbulence dominant
Turbulence ($\tilde{n}_e$) properties	Propagation	Low $\bar{n}_e$	Ion-diamagnetic	
		High $\bar{n}_e$	H: electron-diamagnetic D: ion-diamagnetic	Electron-diamagnetic
	Amplitude	Low $\bar{n}_e$	Amp.(H) < Amp.(D)	Amp.(H) ≈ Amp.(D)
		High $\bar{n}_e$		Amp.(H) > Amp.(D)
	Nonlinear coupling		\	Nonlinear coupling exists

Data availability statement

The data supporting the findings of this study are available in the LHD experiment data repository at https://doi.org/10.57451/lhd.analyzed-data.

Acknowledgments

The authors thank the LHD team members for their great support in 23rd experiment campaign and for the excellent operation of LHD. This work was partially supported by the National Natural Science Foundation of China (Grant Nos. 11820101004 and 12175186), and partly by the National MCF Energy R&D Program (Grant Nos. 2022YFE03070000, 2019YFE03020002 and 2019YFE03040002). This work was also supported by the NIFS general collaboration project, NIFS18KBAP041, NIFS19KLPP057, NIFS20KBAP067, NIFS22KIPH009, NIFS22KIPH010 NIFS22KIPH011, NIFS22KIEE001, and 'PLADyS', JSPS Core-to-Core Program, A. Advanced Research Networks.

ORCID iDs

H. Zhou https://orcid.org/0000-0002-8504-965X
Y. Xu https://orcid.org/0000-0003-4882-647X
M. Kobayashi https://orcid.org/0000-0002-0990-7093
A. Shimizu https://orcid.org/0000-0003-3764-3184
R. Seki https://orcid.org/0000-0002-5364-805X
K. Tanaka https://orcid.org/0000-0002-1606-3204
T. Tokuzawa https://orcid.org/0000-0001-5473-2109
M. Yoshinuma https://orcid.org/0000-0002-5113-9710
Y. Takemura https://orcid.org/0000-0003-3754-897X
H. Takahashi https://orcid.org/0000-0001-6984-9174
K. Ogawa https://orcid.org/0000-0003-4555-1837
J. Cheng https://orcid.org/0000-0002-0496-5542
W. Li https://orcid.org/0000-0003-0663-7638
Y. Luo https://orcid.org/0000-0002-0934-9853
Y.C. Li https://orcid.org/0000-0003-1630-014X
J. Huang https://orcid.org/0000-0003-4179-943X
X.Q. Wang https://orcid.org/0000-0001-8485-895X
H.F. Liu https://orcid.org/0000-0002-0424-645X
H. Liu https://orcid.org/0000-0001-6407-5958
X. Zhang https://orcid.org/0000-0001-8603-4356

References

[1] Ida K. 2023 *Rev. Mod. Plasma Phys.* **7** 23
[2] Xu Y., Hidalgo C., Shesterikov I., Krämer-Flecken A., Zoletnik S., Van Schoor M. and Vergote M. (TEXTOR Team T.) 2013 *Phys. Rev. Lett.* **110** 265005
[3] Bessenrodt-Weberpals M. *et al* 1993 *Nucl. Fusion* **33** 1205
[4] Stroth U. 1998 *Plasma Phys. Control. Fusion* **40** 9
[5] Maggi C.F. *et al* 2019 *Nucl. Fusion* **59** 076028
[6] He Y. *et al* 2022 *Plasma Sci. Technol.* **24** 095102
[7] Horton W. 1999 *Rev. Mod. Phys.* **71** 735
[8] Perkins F.W. *et al* 1993 *Phys. Fluids* B **5** 477
[9] Schissel D.P. *et al* 1989 *Nucl. Fusion* **29** 185

[10] Cordey J.G. *et al* 1999 *Nucl. Fusion* **39** 301
[11] Lorenzini R. and Gobbin M. 2021 *Plasma Phys. Control. Fusion* **63** 114005
[12] Yamada H. *et al* 2019 *Phys. Rev. Lett.* **123** 185001
[13] Tanaka K. *et al* 2019 *Nucl. Fusion* **59** 126040
[14] Tanaka K., Okamura S., Minami T., Ida K., Mikkelsen D.R., Osakabe M., Yoshimura Y., Isobe M., Morita S. and Matsuoka K. 2016 *Plasma Phys. Control. Fusion* **58** 055011
[15] Ohtani1 Y. *et al* 2017 *J. Phys. Soc. Japan* **86** 064501
[16] Yan Z., Gohil P., McKee G.R., Eldon D., Grierson B., Rhodes T. and Petty C.C. 2017 *Nucl. Fusion* **57** 126015
[17] Schneider P.A., Hennequin P., Bonanomi N., Dunne M., Conway G.D. and Plank U. 2021 *Plasma Phys. Control. Fusion* **63** 064006
[18] Silva C., Hillesheim J.C., Hidalgo C., Belonohy E., Delabie E., Gil L., Maggi C.F., Meneses L., Solano E. and Tsalas M. 2016 *Nucl. Fusion* **56** 106026
[19] Gurchenko A.D. *et al* 2016 *Plasma Phys. Control. Fusion* **58** 044002
[20] Ramisch M., Häberle E., Mahdizadeh N. and Stroth U. 2008 *Plasma Sources Sci. Technol.* **17** 024007
[21] Losada U. *et al* 2021 *Plasma Phys. Control. Fusion* **63** 044002
[22] Ohshima S. *et al* 2021 *Plasma Phys. Control. Fusion* **63** 104002
[23] Nakata M., Nunami M., Sugama H. and Watanabe T.-H. 2017 *Phys. Rev. Lett.* **118** 165002
[24] Liu B., Pedrosa M.A., van Milligen B.P., Hidalgo C., Silva C., Tabarés F.L., Zurro B., McCarthy K.J., Cappa A. and Liniers M. 2015 *Nucl. Fusion* **55** 112002
[25] Angioni C. *et al* 2005 *Phys. Plasmas* **12** 040701
[26] Ida K., Nakata M., Tanaka K., Yoshinuma M., Fujiwara Y., Sakamoto R., Motojima G., Masuzaki S., Kobayashi T. and Yamasaki K. 2020 *Phys. Rev. Lett.* **124** 025002
[27] Nakata M., Nagaoka K., Tanaka K., Takahashi H., Nunami M., Satake S., Yokoyama M. and Warmer F. 2019 *Plasma Phys. Control. Fusion* **61** 014016
[28] Takeiri Y. *et al* 2010 *Fusion Sci. Technol.* **58** 482
[29] Osakabe M. *et al* 2001 *Rev. Sci. Instrum.* **72** 590–3
[30] Yoshinuma M., Ida K., Yokoyama M., Osakabe M. and Nagaoka K. 2010 *Fusion Sci. Technol.* **58** 375
[31] Yamada I., Narihara K., Funaba H., Minami T., Hayashi H. and Kohmoto T. 2010 *Fusion Sci. Technol.* **58** 345
[32] Tanaka K., Michael C.A., Vyacheslavov L.N., Sanin A.L., Kawahata K., Akiyama T., Tokuzawa T. and Okajima S. 2008 *Rev. Sci. Instrum.* **79** 10E702
[33] Tokuzawa T. *et al* 2014 *Plasma Fusion Res.* **9** 1402149
[34] Tokuzawa T. *et al* 2018 *Rev. Sci. Instrum.* **89** 10H118
[35] Yokoyama M., Watanabe K. and Nakajima N. 2005 *J. Plasma Fusion Res.* **81** 83–84
[36] Murakami S., Wakasa A., Maa berg H., Beidler C.D., Yamada H. and Watanabe K.Y. (LHD Experimental Group) 2002 *Nucl. Fusion* **42** L19
[37] Tanaka K. *et al* 2021 *Plasma Phys. Control. Fusion* **63** 094001
[38] Yamada H. *et al* 2005 *Nucl. Fusion* **45** 1684–93
[39] SEKI R. *et al* 2011 *Plasma Fusion Res.* **6** 2402081
[40] Goto M., Sawada K., Oishi T. and Morita S. 2016 *Plasma Phys. Control. Fusion* **58** 084001
[41] Beidler C.D. and Hitchon W.N.G. 1994 *Plasma Phys. Control. Fusion* **36** 317
[42] Warmer F. *et al* 2021 *Phys. Rev. Lett.* **127** 225001
[43] Tynan G.R., Fujisawa A. and McKee G. 2009 *Plasma Phys. Control. Fusion* **51** 113001
[44] Kim Y.C. and Powers E.J. 1978 *Phys. Fluids* **21** 1452
[45] Xu Y. *et al* 2011 *Plasma Phys. Control. Fusion* **53** 095015
[46] Tynan G.R., Moyer R.A., Burin M.J. and Holland C. 2001 *Phys. Plasmas* **8** 2691–9
[47] Shats M.G. and Solomon W. 2002 *Phys. Rev. Lett.* **88** 045001
[48] Fujisawa A. 2009 *Nucl. Fusion* **49** 013001
[49] Kobayashi M., Tanaka K., Ida K., Hayashi Y., Takemura Y. and Kinoshita T. 2022 *Phys. Rev. Lett.* **128** 125001